PNAS RESEARCH ARTICLE | BIOPHYSICS AND COMPUTATIONAL BIOLOGY

C-type inactivation and proton modulation mechanisms of the TASK3 channel

Huajian Lin[a,b,1,2], Junnan Li[c,1], Qiansen Zhang[c,1], Huaiyu Yang[c,3], and Shanshuang Chen[a,b,d,e,3]

Edited by Roderick MacKinnon, The Rockefeller University, New York, NY; received November 20, 2023; accepted March 19, 2024

The TWIK-related acid-sensitive K^+ channel 3 (TASK3) belongs to the two-pore domain (K2P) potassium channel family, which regulates cell excitability by mediating a constitutive "leak" potassium efflux in the nervous system. Extracellular acidification inhibits TASK3 channel, but the molecular mechanism by which channel inactivation is coupled to pH decrease remains unclear. Here, we report the cryo-electron microscopy structures of human TASK3 at neutral and acidic pH. Structural comparison revealed selectivity filter (SF) rearrangements upon acidification, characteristic of C-type inactivation, but with a unique structural basis. The extracellular mouth of the SF was prominently dilated and simultaneously blocked by a hydrophobic gate. His98 protonation shifted the conformational equilibrium between the conductive and C-type inactivated SF toward the latter by engaging a cation–π interaction with Trp78, consistent with molecular dynamics simulations and electrophysiological experiments. Our work illustrated how TASK3 is gated in response to extracellular pH change and implies how physiological stimuli might directly modulate the C-type gating of K2P channels.

C-type inactivation | proton modulation | cryo-electron microscopy | electrophysiology | molecular dynamics simulation

Significance

Investigations on the C-type gating of multiple potassium channels have revealed a consistent structural mechanism that deviations in the selectivity filter impair the coordination of potassium ions, in turn inactivating the channel. Given that potassium channels gate in response to physiological stimuli including pH, mechanical force, signaling molecules, and so on, the underlying mechanism by which changes of stimuli are coupled to the C-type gating is largely elusive. Using combined approaches of single-particle cryo-EM, electrophysiology and molecular dynamics simulation, we elucidate an unusual C-type inactivation and proton modulation mechanism of the proton-sensitive TASK3 channel by revealing how extracellular acidification stabilizes the C-type inactivated conformation.

TASK3 is a member of the K2P leak potassium channel family (1). Expressed in excitable cells in the central and peripheral nervous systems (2–7), TASK3 is responsible for extracellular pH-gated background potassium efflux that shapes the resting membrane potential and thereafter influences the cellular excitability (8, 9). Dysfunction of TASK3 is associated with a variety of neuronal pathologies including pain (10–12), depression (13, 14), memory disorders, (15) and Birk–Barel syndrome (16, 17), and TASK3 has shown promising potential as a therapeutic target (10, 18). The gating properties of TASK3 have been extensively characterized by electrophysiology (8, 19–21); however, the underlying gating and modulation mechanisms are elusive due to the lack of structural information. Although TASK3 likely shares a similar overall architecture with the closely related TASK1 (22), additional conformational snapshots corresponding to its functional states are still needed.

Previous studies of Shaker and KcsA potassium channels uncovered two general types of inactivation mechanisms with distinct structural basis (23, 24). Whereas the N-type inactivation with faster kinetics involves channel blockage by its amino-terminus from the intracellular side, the slower C-type inactivation is thought to be underpinned by deviations in the selectivity filter (SF) that impair the coordination of potassium ions (25, 26). Accumulated structural data have revealed that SF deviations attributing to the C-type inactivation involve diverse extent of pinching (23, 27, 28), dilation, (29) or order-disorder transitions in small scales (30, 31); it remains debatable whether the C-type inactivation can be underscored by any alternative form of SF rearrangement. C-type inactivation is modulated by various intracellular or extracellular stimuli, yet the underlying mechanism is poorly known, at least in part due to the complication that C-type inactivation is dependent on extracellular potassium concentration (32, 33) as well as channel gating at the intracellular helical bundle crossing (24, 34–36). Therefore, a productive model system best for mechanistic elucidation of the modulation of the C-type inactivation should be devoid of N-type inactivation, with carefully tuned potassium concentration. K2P channels make such models because they typically lack the intracellular helical bundle crossing necessary for N-type gating, and are gated in response to various stimuli. The C-type gating of K2P channels has been supported by several independent structural studies (30, 37, 38). Consistently, molecules that stabilize the SF have been found to potentiate K2P channels (10, 39). Hereby, extracellular pH-gated TASK3, a typical member of the K2P family, is studied to illustrate whether and how proton modulates the C-type inactivation.

In this study, we present the structural evidence that TASK3 undergoes C-type inactivation in response to acidic pH by a non-canonical mechanism. The C-type inactivation of TASK3 results from unexpected large-scale SF rearrangement and simultaneous formation

Author contributions: H.Y. and S.C. designed research; H.L., J.L., and Q.Z. performed research; H.L., J.L., Q.Z., H.Y., and S.C. analyzed data; and H.L., H.Y., and S.C. wrote the paper.

The authors declare no competing interest.

This article is a PNAS Direct Submission.

[1]H.L., J.L., and Q.Z. contributed equally to this work.

[2]Present address: Chinese Academy of Sciences Center for Excellence in Molecular Plant Sciences, Institute of Plant Physiology and Ecology, Chinese Academy of Sciences, Shanghai 200032, China.

[3]To whom correspondence may be addressed. Email: hyyang@bio.ecnu.edu.cn or chenlab@shsmu.edu.cn.

This article contains supporting information online at https://www.pnas.org/lookup/suppl/doi:10.1073/pnas.2320345121/-/DCSupplemental.

Published April 17, 2024.

of an extracellular obstruction. By combined multidisciplinary approaches including cryo-electron microscopy (cryo-EM), electrophysiology, and MD simulation, we further illustrated how protonation of the proton sensor is coupled to stabilization of the C-type inactivated conformation. The modulation of the C-type inactivation indeed underlies the extracellular pH-dependent inhibition of TASK3; therefore, a potential role of C-type inactivation in the stimulus-dependent modulation is implicated for various other potassium channels.

Results

Overall Structure of Human TASK3. Structural determination of full-length human TASK3 ($TASK3_{FL}$) by cryo-EM is likely challenging due to its poor homogeneity. To overcome this difficulty, we generated a C-terminally truncated construct $TASK3_{1–258}$, which exhibited an identical current-voltage (I-V) relationship and fully reproduced the inhibition by extracellular acidification (Fig. 1 *A* and *B* and *SI Appendix*, Fig. S1), thus justifying its relevance in subsequent structural analyses. $TASK3_{1–258}$ reconstituted into nanodiscs (*SI Appendix*, Fig. S2 *A–G*) produced good contrast when imaged by cryo-EM, allowing structural determination under various conditions. We first investigated a neutral pH and low potassium condition mimicking the extracellular environment (pH 7.4, 5 mM KCl, and 135 mM NaCl) and determined the structure of $TASK3_{1–258}$. Imposition of C2 symmetry resulted in no difference in the reconstructed density map, except for an improved nominal resolution to 3.48 Å, indicating that TASK3 is indeed twofold symmetry related (Fig. 1*C* and *SI Appendix*, Fig. S3 *A–F*). Overall, the molecular architecture of TASK3 is largely consistent with previously reported K2P structures (22, 37–42). Each protomer in the domain-swapped TASK3 dimer contains two homologous pore-forming domains (PDs). The first PD consists of transmembrane helices M1 and M2 flanking an extracellular cap (EC) and a selectivity filter motif (SF1). The second PD is composed of helices M3 and M4, with a homologous selectivity filter motif (SF2) in between, and lacks a prominent extracellular domain (Fig. 1*C* and *SI Appendix*, Fig. S4 *A* and *B*). The M1 helices from two protomers are domain-swapped, presumably stabilizing the dimer (Fig. 1*C*). SF1 and SF2 from both protomers are arranged in pseudo fourfold symmetry, giving rise to a classical potassium SF structure reminiscent of those in classical tetrameric potassium channels such as KcsA (43). Based on the structural conservation between SFs of TASK3 and KcsA, we infer that the five potassium binding sites S0-S4 defined in the high-resolution KcsA structure (43) are also present in TASK3, and are coordinated by carbonyl oxygen atoms of the SF motifs (TIGYG in SF1 and TIGFG in SF2) along the channel axis (Fig. 1*D* and *SI Appendix*, Fig. S5*A*). Consistently, strong density for potassium is present at all S0-S4 sites, indicating that the SF is in a conductive state (*SI Appendix*, Fig. S5*A*).

TASK3 and closely related TASK1 share a structural specification, termed the "X-gate" (22), where kinked M4 helices dimerize

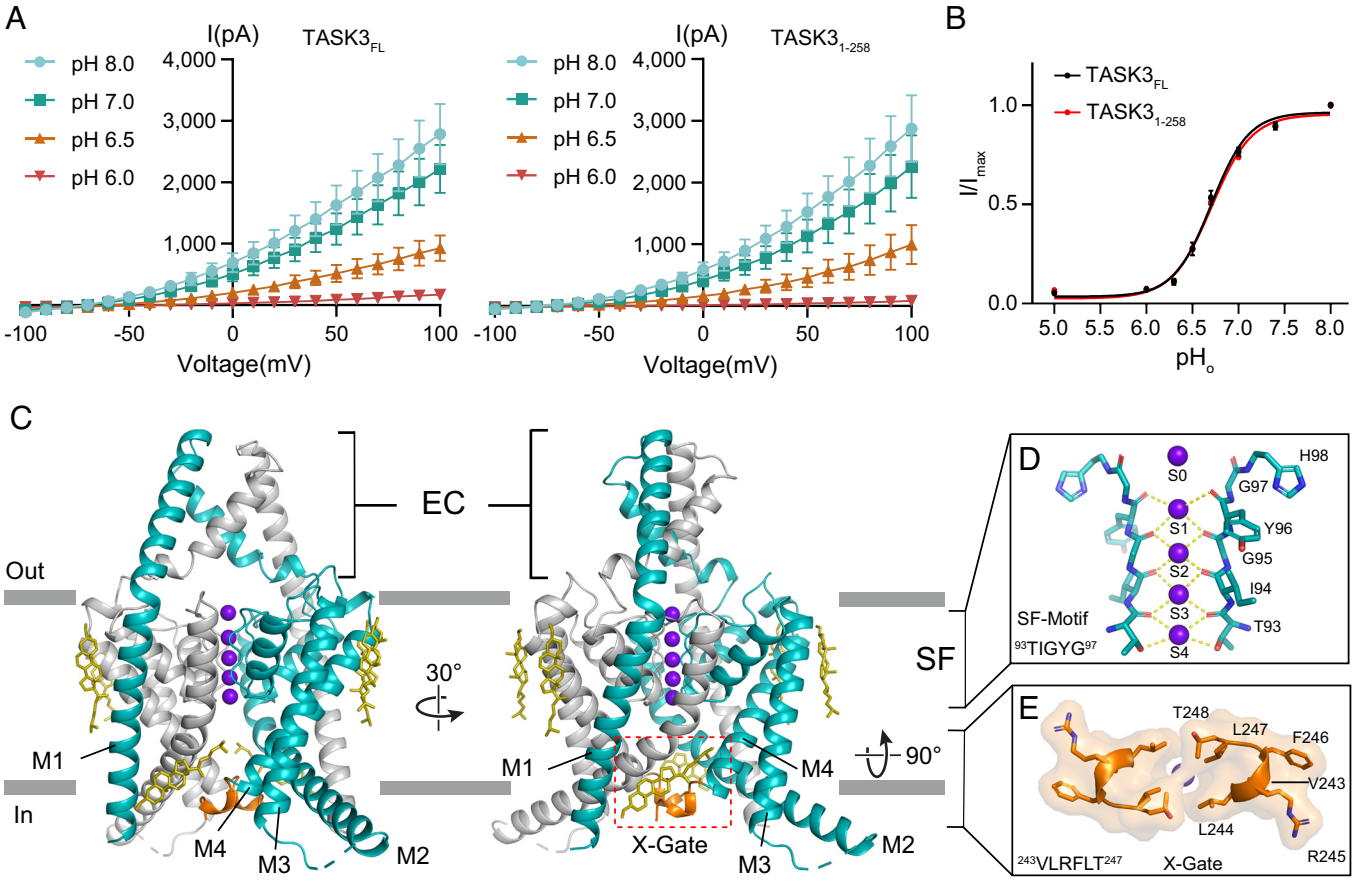

Fig. 1. Function and structure of the TASK3 channel. (*A*) Current-voltage relationships of $TASK3_{FL}$ (*Left*) and $TASK3_{1–258}$ (*Right*) expressed in CHO-K1 cells in response to extracellular pH (pH_o). (*B*) Proton inhibition of $TASK3_{FL}$ and $TASK3_{1–258}$. Data points represent averages of whole-cell currents recorded with the membrane potential clamped at 0 mV, normalized to that recorded at pH 8.0. Error bars indicate the SEM (n ≥ 5). Current-pH_o relationships were fitted with the Hill equation. (*C*) Cryo-EM structure of $TASK3_{1–258}$ viewed in parallel to the membrane. Two protomers are colored in teal and gray. The X-gate is colored in orange and indicated by a red dashed frame. Coordinated potassium ions are represented by purple spheres. Cholesterol/CHS molecules bound to TASK3 are shown as olive sticks. Transmembrane helices M1-M4 and the extracellular cap (EC) domain are labeled. (*D*) Magnified view of the selectivity filter motif SF1 shown in stick models. SF2 has been omitted for clarity. (*E*) Enlarged bottom–up view of the X-gate.

to obstruct the channel entrance at the intracellular ends (Fig. 1 *C* and *E*). The M4 dimerization interface in the TASK3 X-gate is not as extensive as in TASK1, with disordered residues 249-258 missing from our TASK3 structure (*SI Appendix*, Fig. S6). Notably, there is clear density putatively for a molecule of either cholesterol (supplemented with lipids during nanodisc reconstitution) or its derivative cholesterol succinate (CHS, supplemented with detergent during purification) on each side of the X-gate, in close proximity to the M4 helices (Fig. 1*C* and *SI Appendix*, Fig. S4*A*). We speculate that the X-gate of TASK3 is subject to cholesterol modulation and that the X-gate in our structure (Fig. 1*E*) is closed due to the high concentrations of CHS or cholesterol used during sample preparation. In conclusion, the TASK3 structure determined at neutral pH represents an SF-conductive, X-gate closed conformation.

C-type Inactivation of TASK3 upon Acidification. Next, we attempted to uncover the structural rearrangements underlying TASK3 inhibition by acidification. TASK3 structure was similarly determined at low pH (pH 6.0, 5 mM KCl, and 135 mM NaCl) at 3.68 Å resolution (*SI Appendix*, Fig. S7), the analysis of which revealed unexpected large-scale rearrangements in the SF, flanking residues Thr93 to Pro101 in SF1 and Thr199 to Val206 in SF2 (Fig. 2 *A* and *B*). The carbonyl oxygens of Gly-(Tyr/Phe)-Gly in the conserved SF motif were deviated from positions ideal for mimicking the hydration of potassium ions by ways of main chain flipping (Fig. 2 *B* and *C*), where the flexibility of glycine residues was likely critical. Because these carbonyl oxygens mimic the hydration of potassium ions bound at S1-S2 sites in the conductive SF, deviations in these oxygens were expected to impair potassium coordination and thus render the SF nonconductive, a classical gating mechanism known as C-type inactivation. Indeed, potassium density was much weaker at S1-S2 sites than at S3-S4 sites (*SI Appendix*, Fig. S5*B*), the latter of which remained intact given unaltered Thr-Ile in the SF motif (Fig. 2*C*). Although the lack of potassium density at S1-S2 sites was consistent with the C-type inactivation, hampered potassium permeation required further structural explanation given that the mouth of the SF was not restricted but prominently dilated (Fig. 2*C*). Remarkably, the side chains of Tyr96 and Phe202 in the SF motifs, poised in parallel with the membrane in the SF-conductive state, were now reoriented to be along the channel axis as a consequence of main chain flipping, a process analogous to the closing of a bloomed flower with four pedals represented by the aromatic side chains (Fig. 2 *D* and *E*). Stabilized by hydrophobic interactions, these aromatic side chains acted as an extracellular gate, obstructing the potassium permeation pathway (Fig. 2 *D* and *E*). The rearranged SF retained its twofold symmetry, indicating that the main chains of SF1 and SF2 flipped concomitantly; otherwise, a steric clash would occur between any aromatic side chain of Tyr96 or Phe202 from a flipped SF and the main-chain of an adjacent unflipped SF. Thus, it is likely that the hydrophobic extracellular gate closure results from concerted rearrangements of SF1 and SF2. Taken together, we conclude that the TASK3 structure determined under the acidic condition represents an SF nonconductive,

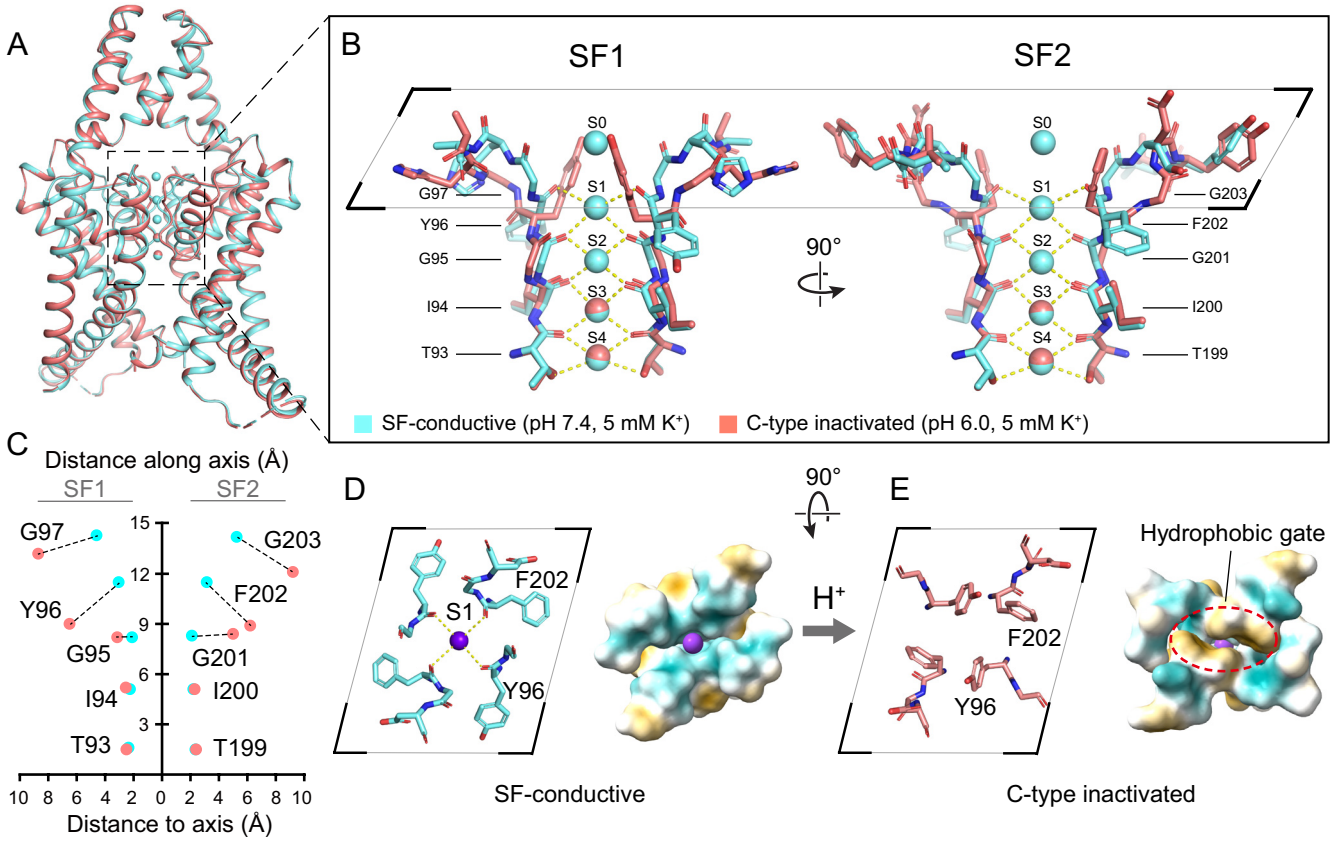

Fig. 2. C-type inactivation of TASK3 upon extracellular acidification. (*A*) Structural superposition of TASK3 determined at pH 7.4 (cyan) and pH 6.0 (salmon) under low potassium conditions (5 mM KCl and 135 mM NaCl). (*B*) Orthogonal views of the selectivity filter motifs (SF1 and SF2) shown in stick models. Coordinated potassium ions are indicated by spheres in consistent color code. (*C*) Displacements of carbonyl oxygens in the SF motifs upon the C-type inactivation. Distances along and to the channel axis are plotted with the position of S4 set as the origin. Positions of carbonyl oxygens from the SF-conductive or C-type inactivated structures were shown as cyan or salmon dots, respectively. (*D*) and (*E*) Top–down views of the extracellular mouths of the conductive (*D*) and the C-type inactivated SF (*E*) showing formation of a hydrophobic gate upon protonation. Stick and surface models are shown side by side, the latter colored according to hydrophobicity, with hydrophilic and hydrophobic regions colored in cyan and yellow, respectively.

C-type inactivated conformation, and TASK3 channel undergoes C-type inactivation via a proton-dependent mechanism.

Notably, C-type inactivation of different potassium channels varies in their structural basis. TASK3 in the C-type inactivated conformation is structurally distinct in several aspects, which underpins its unique inactivation mechanisms. First, the SF dilation observed in C-type inactivated TASK3 is to a much greater extent than that in TASK2 (37), TREK1 (30, 44), TREK2 (42) and TWIK1 (38), as contrasted by dramatically displaced SF carbonyl oxygens in TASK3 (Fig. 2*C*) and only modest displacements of corresponding atoms in other K2P channels (*SI Appendix*, Fig. S8 *A–C*). Second, despite the conservation of Gly-(Tyr/Phe)-Gly in the SF motif, formation of a hydrophobic extracellular gate with Tyr/Phe is observed, highlighting the functional importance of these aromatic residues, which also likely contributes to the concerted motion of four SF motifs. Third, main chain flipping of the SF motif was only observed in C-type inactivation of TASK3 and TWIK1 channels (*SI Appendix*, Fig. S8*D*). C-type inactivation of TWIK1 involves global rearrangements including EC shift and fenestration dilation; by contrast, structural rearrangements of TASK3 are domestic, involving only the SF motif and a few adjacent residues. Last but not least, the C-type inactivated SF of TASK3 is stabilized by newly engaged side chain interactions, the details of which are described below. Taken together, our structural findings add up to the existing knowledge about C-type inactivation mechanisms, and underscore the diversity in the structural bases for the C-type inactivation of different potassium channels.

Mechanisms for Proton Sensing and Modulation of C-type Inactivation. With both the SF-conductive and C-type inactivated structures in hand, we can now begin to deduce the mechanisms by which channel protonation is coupled to conformational changes in the SF. Histidine residues, due to their imidazole side chains, feature a pKa that overlaps with the physiological pH range, and are therefore often implicated in pH-dependent protein regulation. Of the nine histidine residues in $TASK3_{FL}$, four are present in $TASK3_{1–258}$ and all are exposed to the extracellular environment. Little change was observed in His33, His72 or His188, or in their interacting partners upon acidification, suggesting that they may not be the proton sensor. In contrast, His98, which is well conserved among the TASK subfamily and the acid-sensitive TWIK1, was previously shown to be critical for proton sensing in TASK3 (1, 45). In the SF-conductive state, His98 is involved in hydrogen bond interactions with Thr89 through one water molecule, and with Gln77 and Gly82 through another (Fig. 3*A*). In the C-type inactivated state captured at acidic pH, His98 is substantially shifted away from the channel axis and is directly hydrogen bonded to Gln77 and Gly82 (Fig. 3*B*). Remarkably, the shifted imidazole group of His98, likely protonated at the given pH, established a cation–π interaction with the indole side chain of Trp78, with a distance of ~4.3 Å from the protonated nitrogen to the benzene ring (Fig. 3*C*). We therefore hypothesize that the cation–π interaction between His98 and Trp78 plays a role in stabilizing the C-type inactivated conformation in a protonation-dependent manner.

To test whether the proposed cation–π interaction between His98 and Trp78 is critical for proton modulation of TASK3, we performed electrophysiological experiments to examine various TASK3 mutants for their responses to decreases in pH. Indeed, mutation of His98 to acidic aspartate or to neutral asparagine rendered the TASK3 channel much less sensitive to extracellular acidification, consistent with the notion that His98 is the proton

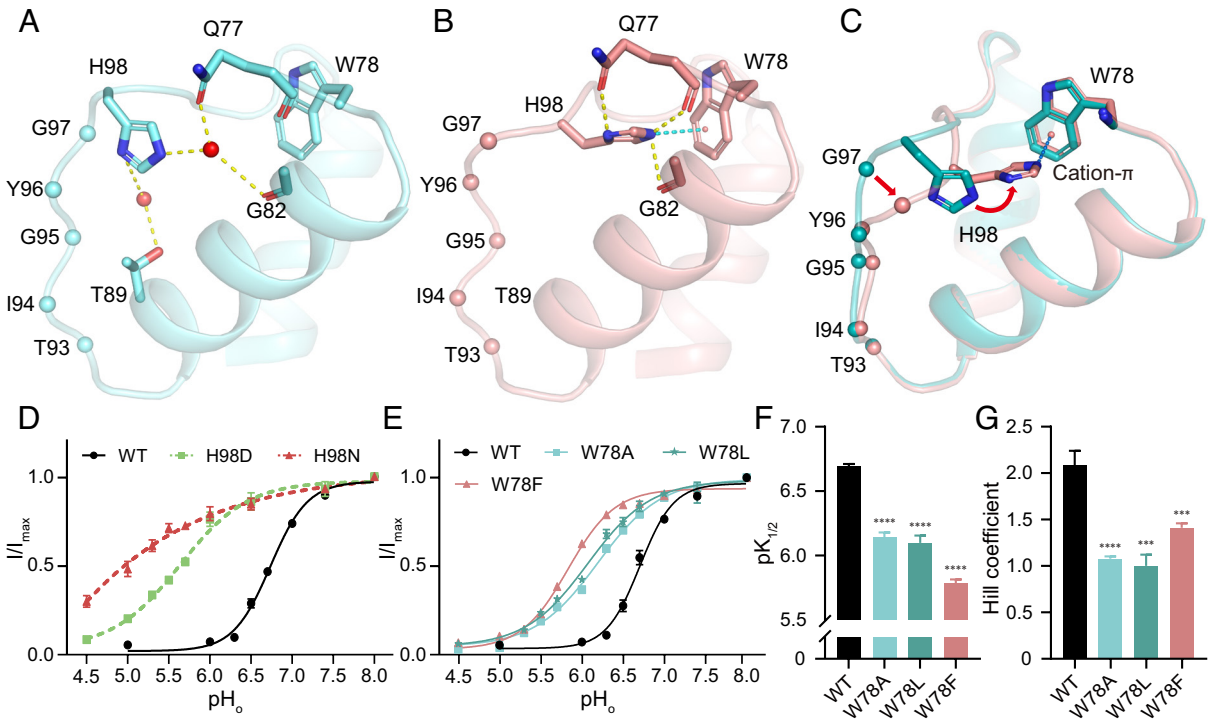

Fig. 3. Structural basis for protonation-dependent SF rearrangements. (*A*) Hydrogen-bond network involving Gln77, Gly82, Thr89, and His98, in the conductive SF (cyan) indicated by yellow dashed lines. Water molecules bridging hydrogen bonds are shown as red spheres. (*B*) Protonated His98 is in cation–π interaction with Trp78 and is in hydrogen bond interactions with Gln77 and Gly82 in C-type inactivated SF (salmon). The cation–π interaction is indicated by a cyan dashed line. (*C*) Superposition of the conductive and C-type inactivated SF highlighting the main chain rearrangements and His98 movement (red arrow). (*D*) and (*E*) Dose–responses to extracellular protons for $TASK3_{FL}$, as well as His98 (*D*) and Trp78 (*E*) mutants (n ≥ 5). Data are fitted with the Hill equation. Because maximum inhibitions were not faithfully achieved with His98 mutants, fitting with Hill equation (dotted lines) could produce inaccurate $pK_{1/2}$ and Hill coefficient, hence not reported. (*F*) and (*G*) The $pK_{1/2}$ (*F*) and Hill coefficient (*G*) values of wild-type (WT) $TASK3_{FL}$ and Trp78 mutants. Columns and error bars represent the means and their SEs, respectively. Significance was assessed by Student's *t* test. ****$P < 0.0001$, *$P < 0.05$, n.s.: not significant.

sensor (1, 45) (Fig. 3*D* and *SI Appendix*, Fig. S9). In addition, substitution of Trp78 with alanine, leucine or phenylalanine led to significant decreases in the pK1/2 values to 6.14 ± 0.04, 6.10 ± 0.06 or 5.78 ± 0.03, respectively, and reductions in the Hill coefficient to 1.08 ± 0.03, 1.00 ± 0.12 or 1.41 ± 0.05, respectively, when compared to the pK1/2 value of 6.69 ± 0.02 and Hill coefficient of 2.08 ± 0.16 determined with wild-type TASK3 (Fig. 3 *E*–*G* and *SI Appendix*, Fig. S9). These results highlight the importance of Trp78 in proton inhibition of the channel and further suggest that the cation–π interaction contributes, at least in part, to the cooperativity. Taken together, the blunted pH sensitivity observed with the His98 or Trp78 mutants supported the role of the proposed cation–π interaction in stabilizing the C-type inactivated state.

Although Trp78 is strictly conserved throughout the K2P family, and His98 is conserved in the proton-sensitive TASK1, TASK3, TASK5, and TWIK1 channels, this cation–π interaction has never been observed in any other K2P structure. Therefore, this unconventional form of C-type inactivation may serve to inspire further structural and functional investigations to find out whether the gating and modulation mechanisms of TASK3 are shared by other members of the K2P family.

His98 Deprotonation Is Sufficient to Restore a Conductive SF. To illustrate whether and how a canonical SF-conductive TASK3 structure can be restored from the C-type inactivated conformation, we carried out MD simulations. These simulations were initiated from the C-type inactivated structure, with the protonation state of the putative pH sensor His98 being the only variable among repeated simulations. The distance between Cα atoms of Gly97 from the opposite protomers, which represents the most dilated position in the inactivated SF, was monitored to reflect the change in the SF (Fig. 4*A*). Additionally, the proximity between His98 and Trp78 within a protomer was monitored to reflect the cation–π interaction unique to the C-type inactivated state (Fig. 4*A*). In simulations where His98 was set to the protonated state, the SF remained in the C-type inactivated conformation (*SI Appendix*, Fig. S10 *A*–*C*). In contrast, in simulations where His98 was deprotonated, the C-type inactivated conformation remained stable only for the first 30 to 90 ns. Thereafter, His98 retreated from Trp78 and the distance between opposing Gly97 decreased, indicating the disruption of the cation–π interaction and the restoration of a conductive SF. At the end of the simulations with deprotonated His98, the Gly97-Gly97 and His98-Trp78 distances were converged to ~10 Å and ~12 Å, respectively, in agreement with those obtained from the SF-conductive structure (Fig. 4*B*). To confirm that the SF-conductive state was indeed achieved, the last frame of each simulation was compared with the cryo-EM structure (*SI Appendix*, Fig. S10*D*). Since symmetry is not mandatory, the four pore loops can diverge during each of the three independent simulations, resulting in a final total of 12 pore loop conformational snapshots. When each pore loop structure was individually aligned with the counterpart of the cryo-EM structure of the conductive SF, the Cα rmsd values were less than 1 Å for 9 out of 12 pore loops (*SI Appendix*, Table S1), consistent with the structural observation that all four pore loops were simultaneously rearranged to achieve the SF-conductive state. These MD simulations not only validated the C-type inactivated structure of the TASK3, but also demonstrated that His98 deprotonation alone is sufficient to trigger the conformational transition necessary to restore a conductive SF.

To gain further insight into the simulated structural arrangements, we plotted a probability heat map against the Gly97-Gly97 and His98-Trp78 distances (Fig. 4*C*), and employed cluster analysis to identify an intermediate conformation between the cryo-EM determined SF-conductive and C-type inactivated states (Fig. 4*D*). During the simulation, rearrangements in the main chain carbonyl oxygens of Tyr96, Gly97 and His98 created a pocket to accommodate the side chain of Phe202, supporting how the hydrophobic extracellular gate was opened and subsequently stabilized. The

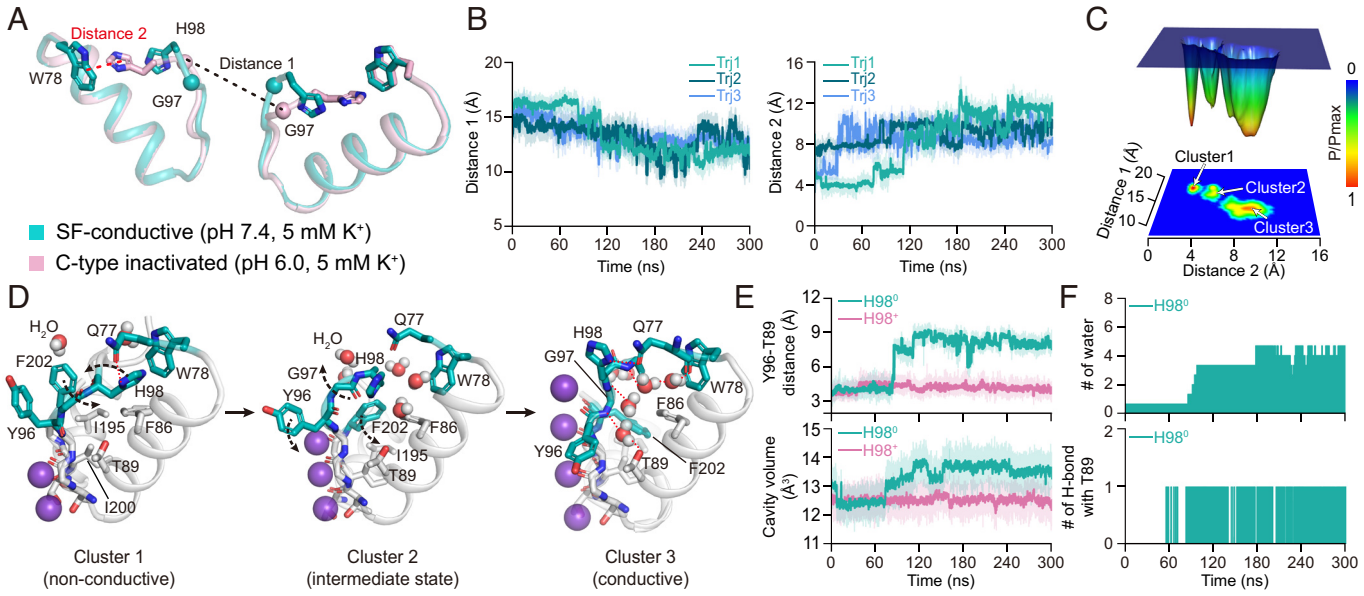

Fig. 4. MD simulations elucidating the SF conformational transition from the C-type inactivated to the SF-conductive state upon His98 deprotonation. (*A*) Superposition of the conductive (cyan) and C-type inactivated (salmon) SF structures, where Distance 1 between the Cα atoms of the opposite Gly97 and Distance 2 between the side chains of His98 and Trp78 are indicated by black and red dashed lines, respectively. (*B*) Distance 1 and Distance 2 in three independent MD simulation trajectories (Trj 1-3). (*C*) Probability heat map against Distance 1 and Distance 2. The probability was normalized to the most abundant conformation. (*D*) Distinct SF conformations revealed by cluster analysis of the probability map, including the C-type inactivated state (Cluster 1), an intermediate state (Cluster 2), and the conductive state (Cluster 3). Potassium ions and water molecules are shown as purple and red spheres, respectively. Key residues are highlighted in color. Dashed arrows indicate the directions of residue movements. (*E*) Distance between hydroxyl oxygen of Thr89 and carbonyl oxygen of Tyr96, as well as volume of the cavity formed by Trp78, Thr89, Tyr96, Gly97, and His98 in MD simulations. (*F*) Number of water molecules in the cavity and hydrogen bond with Thr89 in MD simulations.

imidazole group of His98 moved away from Trp78, leaving a cleft to be filled by a water molecule. Wedged between Tyr96 and Thr89, this water molecule reorganized the local hydrogen bond network. Further hydration of this cleft expanded the cavity surrounded by Trp78, Thr89, Tyr96, Gly97, and His98 to ~14 Å^3 (Fig. 4*E*). Finally, the SF-conductive state was achieved when the cavity was fully hydrated with five water molecules (Fig. 4*F*). In summary, the cation–π interaction between His98 and Trp78 acts as a floodgate, whose "opening" allows hydration of the cavity between the SF motif and the pore helix (Fig. 5). The swelling of the cavity facilitates the reorganization of a hydrogen bond network, which is essential for the restoration of a conductive SF.

Extracellular Potassium Antagonizes Proton-Induced C-Type Inactivation. C-type inactivated SF of TASK3 features compromised potassium binding site S0-S2 in proximity to the extracellular side, consistent with the notion that C-type inactivation is dependent on extracellular potassium concentration (32, 33). Indeed, it has been suggested that TASK3/TASK1 may function to sense extracellular potassium concentration and thereby regulate aldosterone secretion in adrenal glomerulosa cells (46). We hereby employed electrophysiology to test the hypothesis that proton inhibition of TASK3 would be attenuated when the extracellular potassium concentration is elevated. As expected, only 25.6% inhibition of the macroscopic TASK3 current was observed in whole-cell patch clamp recordings upon acidification from pH 7.4 to 6.0 with the external potassium concentration increased to 200 mM (*SI Appendix*, Fig. S11*A*). By contrast, in control experiments where TASK3 currents were recorded near physiological potassium concentration (5 mM externally), perfusion with an acidic external buffer (pH 6.0) resulted in a much more profound depression in TASK3 current (91.9%), whereas perfusion back into neutral external buffer (pH 7.4) largely rescued channel activity (*SI Appendix*, Fig. S11*B*). A similar extent of inhibition was observed when 145 mM extracellular potassium was used instead (25.1%), or when TASK3$_{1–258}$ was used instead of TASK3$_{FL}$ (24.2%) (*SI Appendix*, Fig. S11 *C* and *D*), in agreement with a previous study (19). To confirm that extracellular potassium antagonizes the proton-dependent C-type inactivation of TASK3, we determined the cryo-EM structures of TASK3 at neutral (pH 7.4) and acidic (pH 6.0) conditions, separately combined with a high potassium concentration (200 mM), resulting in reconstructions at 3.0 Å and 3.4 Å resolutions, respectively (*SI Appendix*, Figs. S12 and S13). The structures were near identical, with an all-atom rmsd of 0.05 Å (*SI Appendix*, Fig. S14*A*), and highly consistent with the SF-conductive state described above (*SI Appendix*, Fig. S14*B*). Unambiguous density was observed for potassium ions at S0-S4 sites in both reconstructions, indicating a conductive SF (*SI Appendix*, Fig. S5 *C* and *D*). Despite extensive effort in single-particle analysis, we did not observe any alternative SF conformation or compromised potassium density in subset of particles resulted from 3D-classification, supporting the hypothesis that external potassium in high concentrations prevents proton-induced C-type inactivation described above under a low potassium condition.

Next, we employ MD simulation to further test whether high concentration of extracellular potassium attenuates the C-type inactivation of TASK3 by stabilizing the SF-conductive conformation. The following sets of MD simulations were initiated using the SF-conductive structure with His98 set to be protonated in the presence of high or low extracellular potassium concentrations (200 mM or 5 mM KCl, respectively). Indeed, the SF structure was stabilized in the conductive conformation at the high potassium condition (*SI Appendix*, Fig. S10 *E* and *F*), thus supporting our hypothesis. As control experiments, SF rearrangements to nonconductive conformations recapitulated the C-type inactivation in the MD simulations at the low potassium condition (*SI Appendix*, Fig. S10 *G* and *H*). Interestingly, cluster analysis of a probability heat map derived from the MD simulation trajectories revealed an intermediate conformation (*SI Appendix*, Fig. S10 *I* and *J*) consistent with that found in MD simulations recapitulating reverse process described above (Fig. 4*D*), thus supporting its relevance. However, future functional validations are still required to further validate such an intermediate state, which may provide opportunities for future development of pharmacological tools.

Discussion

C-type gating is thought to be the principal gating mechanism for the majority, if not all, of the K2P family. Our work illustrated how TASK3 undergoes C-type inactivation upon extracellular acidification by revealing the SF rearrangements that disrupt the S0-S2 potassium sites and establish a hydrophobic gate. The reverse process, that is, the reestablishment of the conductive SF from the C-type inactivated conformation occurred spontaneously on condition of deprotonated proton sensor His98 during MD simulations, meanwhile revealing an additional intermediate state. For more than a decade, the structural basis of the C-type

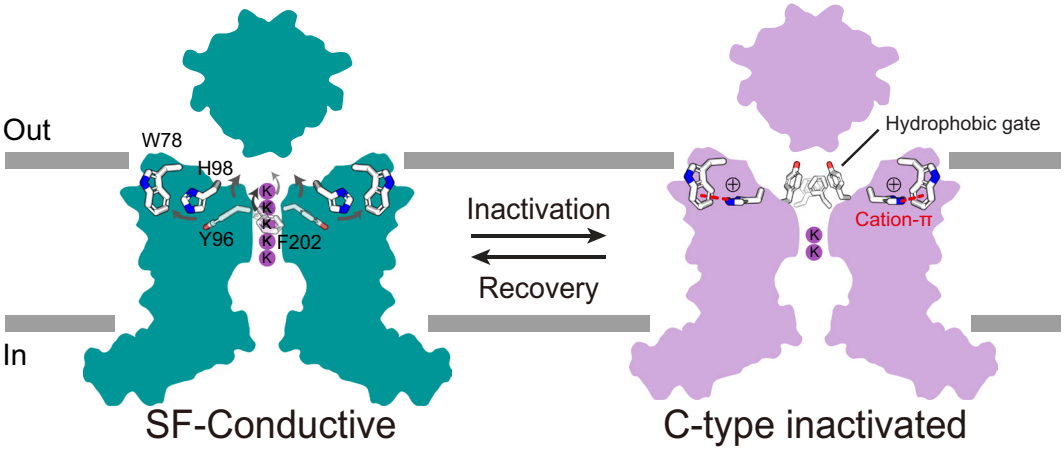

Fig. 5. Model for the pH-sensitive C-type gating of TASK3. At acidic pH, the proton sensor His98 forms a cation–π interaction with Trp78, thus stabilizing the SF in a C-type inactivated conformation, where potassium binding sites are compromised and channel exit is blocked by a hydrophobic extracellular gate. When the pH becomes neutral or higher, the cation–π interaction ceases upon His98 deprotonation. Main chain flipping of the SF motif not only restores all potassium binding sites, but also opens the hydrophobic extracellular gate, thereby achieving the SF-conductive state.

inactivation has been described as small-scale SF rearrangements that impair the coordination of potassium ions (30, 37, 38, 42). Despite the sequential and the structural conservation of SF among highly diverse families of potassium channels, our study revealed that the C-type inactivation can be achieved differently where structural rearrangements involving main chain flipping caused prominent dilation of the SF mouth obstructed by flipped aromatic residues within the SF motif. Moreover, the C-type inactivated conformation is stabilized by cation–π interactions between protonated His98 and Trp78, offering mechanistic insights that extracellular pH modulates TASK3 by tuning the equilibrium between the SF-conductive and C-type inactivated states.

Besides the SF, X-gate must also be taken into consideration in the context of channel gating and modulation mechanisms. While C-type gating may be a common mechanism shared by most potassium channels, X-gate is thought to be present only in the closely related TASK1, TASK3, and TASK5 channels rather than a paradigm for the K2P family. Originally discovered in the crystal structure of TASK1, X-gate has been shown to be important to channel gating, with mutations in X-gate altering channel conductivity. The mechanisms of X-gate and modulation are still unclear, largely due to the lack of an open X-gate structure. In TASK3, closed X-gate was found in direct contact with putative CHS/cholesterol molecules in all pH and potassium conditions tested, consistent with the findings in TASK1, suggesting that the X-gate may be modulated by cholesterol metabolism in vivo. We further hypothesize that CHS/cholesterol stabilizes the closed X-gate and is incompatible with an open X-gate. Indeed, when performing single-particle analysis for data collected in the acidic pH and low potassium condition, we noticed an unusual heterogeneity in the X-gate conformation, which was subsequently resolved by means of 3D classification (*SI Appendix*, Fig. S15). In addition to the closed X-gate formed by kinked M4 helices, we isolated a putative open conformation with straight M4 helices, which are probably sterically incompatible with the CHS/cholesterol sites (*SI Appendix*, Fig. S16), supporting our hypothesis. It should be noted that all our structures were obtained in the presence of excess CHS/cholesterol, which may have shifted the open-closed equilibrium of the X-gate. Despite extensive efforts in single-particle analyses of cryo-EM data collected in other conditions, such conformational heterogeneity was only found with the condition leading to C-type inactivation, suggesting that there may be an allosteric interplay between the two gates analogous to that found between the filter and the helical bundle crossing in Shaker and KcsA channels (24, 34).

A third possible gating mechanism of TASK3 is by lipid insertion into the side fenestration, as similar mechanisms have been proposed for TWIK1, TRAAK, TREK1, and TREK2 (38, 47–49). Indeed, we observed an alkyl chain-like density for unknown molecules copurified with TASK3 (*SI Appendix*, Fig. S4*A*). Extending from the central vestibule through the fenestration to the peripheral lipid environment, the density appeared stronger upon b-factor sharpening, suggesting intrinsic flexibility or heterogeneity. Similar alkyl chain-like densities have been reported to clog the fenestration in a number of K2P structures, but their precise molecular nature remains elusive. As the fenestration and the vestibule are promising "druggable" sites (50), copurified molecules occupying these sites may play an important role in shaping the pharmacological profiles of the K2P family.

The TASK3 structures in various conformational states not only elucidated the proton-dependent inactivation mechanism, but also provided a framework for future pharmacological advances. Candidate agonists and antagonists could be designed, optimized, or selected based on their potential capability to stabilize the SF-conductive and nonconductive states, respectively. Future efforts in structural determination of TASK3 in complex with agonists or antagonists are needed in order to better understand channel gating mechanisms as well as structure-based pharmacology.

Materials and Methods

Constructs. For electrophysiological studies, the full-length human TASK3 ($TASK3_{FL}$, NM_001282534.2) and C-terminally truncated $TASK3_{1–258}$ (residues 1 to 258) were cloned into the pcDNA3.1 vector. For large-scale overexpression, $TASK3_{1–258}$ was cloned into pBacMam vector to be in tandem fusion with a 3C cleavage site, an eGFP, and a strep tag at the C-terminus. Site-directed mutagenesis was performed according to standard protocols.

Cell Culture. Sf9 cells (Sino Biological) were cultured in ESF921 media (Expression Systems) in suspension without FBS or any antibiotic at 27 °C in an orbital shaker with gentle shaking at 110 rounds per minute (rpm). Expi293F cells (Thermo Fisher) were cultured in Union-293 media (Union Biotech) in suspension free of FBS or antibiotics at 37 °C, 5% (v/v) CO_2 in an orbital shaker with gentle shaking at 110 rpm. Cell density and viability were determined by imaging trypan blue-stained cells with a cell counter (Count Star, Thermo Fisher). CHO-K1 cells (Gibco) were cultured in DMEM/F12 medium (Gibco) supplemented with 10% (v/v) fetal calf serum (Gibco) and 1% (v/v) penicillin-streptomycin (Gibco). Cells were incubated in 35-mm culture plates at 37 °C with 5% (v/v) CO_2.

Electrophysiology. CHO-K1 cells cultured in six-well plates were transiently transfected when 80 to 90% confluency was reached. For each transfection, 1.5 μg pcDNA-TASK3 and 1.0 μg pEGFP-N1 plasmid were mixed with 5 μL Lipofectamine 3000 (Invitrogen) and 5 μL P3000 (Invitrogen) before being added to the cells according to the manufacturer's instructions. After 24 to 48 h, successfully transfected cells indicated by eGFP expression were used in subsequent electrophysiological recordings.

Whole-cell electrophysiological recordings were performed at room temperature using standard voltage-clamp technique with a HEKA EPC-10 USB amplifier, with channel currents filtered at 2 kHz and digitized at 10 kHz. Patch pipettes (World Precision Instruments) were pulled to a resistance of 3 to 5 MΩ. With a holding potential of −80 mV, outward currents of TASK3 were elicited by voltage ramps from −100 to +100 mV over 1 s. The internal pipette solution consisted of 145 mM KCl, 1 mM $MgCl_2$, 5 mM EGTA, and 10 mM Hepes (pH 7.3 with KOH), whereas the external bath solution contained 140 mM NaCl, 5 mM KCl, 2 mM $CaCl_2$, 1 mM $MgCl_2$, and 10 mM glucose and was buffered with 10 mM Hepes (pH 8.0, 7.4 or 7.0 with NaOH). Hepes was replaced by MES (pH 6.7, 6.5, 6.3, 6.0, 5.7, or 5.5 with NaOH) or by citric acid (pH 5.3, 5.0, or 4.5 with NaOH) in acidic solutions. To test the effect of high extracellular K^+ on TASK3 currents, the 145 mM K^+ bath solution was obtained by equimolar replacement of Na^+ by K^+ and the 200 mM K^+ bath solution contained 200 mM KCl, 2 mM $CaCl_2$, 1 mM $MgCl_2$, 10 mM glucose, and 10 mM Hepes (pH 7.4 with NaOH) or MES (pH 6.0 with NaOH) without NaCl addition. I-V relationship was sampled every 50 ms (hence 21 data points in each 1,000-ms ramp) and I-V curves were obtained by connecting neighboring data points. The dose–response curve for extracellular proton inhibition of TASK3 was fitted with Hill Equation: $y = 1/[1 + (K_{1/2}/[H^+]^n)]$. Patch clamp data were processed by Clampfit 10.4, followed by analyses using GraphPad Prism 8.0.2. All data are presented as mean ± SEM.

Expression and Purification. Overexpression of TASK3 was carried out using the BacMam system according to standard protocols. Briefly, the pBacMam-TASK3 plasmid was transformed into DH10Bac *Escherichia coli* for bacmid recombination. Positive clones were selected by plating transformed DH10Bac cells on LB plates supplemented with 50 μg/mL kanamycin, 10 μg/mL tetracycline, 7 μg/mL gentamicin, 40 μg/mL isopropyl β-D-thiogalactoside (IPTG) and 100 μg/mL Bluogal. Bacmid DNA extracted from bacterial culture inoculated with a single positive colony (white) was transfected into Sf9 cells grown in adherence using transfection reagent Cellfectin II (Thermo Fisher Scientific) and the standard protocol provided by the manufacturer to generate P1 virus. P1 virus was harvested 4 d after transfection by passing the cell media through a 0.2 μm filter. P2 virus was thereafter produced by infection of Sf9 cells (1.2×10^6 cells/mL in suspension)

with P1 virus at 1:5000 (P1 virus: Sf9 suspension, v/v). P2 virus was also harvested 4 d after infection by filtration of the cell media through a 0.2 μm filter. Fetal bovine serum (FBS) was added to P1 and P2 virus prior to filtration for extended preservation at 4 °C until use (51).

Expi293F cells cultured in suspension at a density of 2.5 to 3.5 × 10^6 cells/mL were infected with P2 virus (30 to 40 mL of virus per flask containing 0.8 L of Expi293F cells). After 8 to 24 h, 10 mM sodium butyrate was added, and the cell culture temperature was lowered to 30 °C. Cells were harvested 60 to 90 h after infection by centrifugation for 12 min at 4,000 rpm (JLA-8.1 rotor, Beckman Coulter). Cell pellets were washed with buffer containing 20 mM Hepes pH 7.4 and 150 mM KCl and stored at −80 °C.

For protein purification, thawed cells were resuspended for solubilization in lysis buffer [20 mM Hepes pH 7.4, 200 mM KCl, 1 mM dithiothreitol (DTT), 1.5% (m/v) DDM and 0.2% (m/v) CHS] supplemented with protease inhibitors (1 mM phenylmethanesulfonyl fluoride, 0.2 μM aprotinin, 2 μg/mL leupeptin, 2 μM pepstatin A). Cells were solubilized for 2 to 3 h at 4 °C with gentle agitation, before being subjected to ultracentrifugation at 40,000 rpm for 1 h (Ti45 rotor, Beckman Coulter). The supernatant was passed through a 0.22 μm filter, and then incubated with Streptactin XT resin pre-equilibrated with buffer containing 20 mM Hepes pH 7.4 and 150 mM KCl at 4 °C for 30 min with gentle rocking. The mixture was then transferred to a gravity flow column, and the resin was washed with 4 column volumes of running buffer (20 mM Tris pH 7.4, 200 mM KCl, 1 mM DDM, 0.2 mM CHS, and 1 mM DTT). Protein eluted with elution buffer (running buffer supplemented with 150 mM biotin) was concentrated and subjected to size-exclusion chromatography (SEC) using a Superose 6 column (10/300 GL, GE Healthcare) and the same running buffer. The peak fractions were collected and concentrated to 2 to 3 mg/mL, and the purity was examined by SDS-PAGE and western blot.

Nanodisc Reconstitution. The membrane scaffold protein MSP1D1 was expressed in BL21 (DE3) pLysS *E. coli* cells. Cells were grown in LB media at 37 °C and protein expression was induced with 0.3 mM IPTG at 18 °C. Harvested cells were resuspended in lysis buffer containing 20 mM Tris-HCl pH 8.0, 150 mM NaCl, 5% (v/v) glycerol, 1 mM DTT, and 0.05% (v/v) Tween-20, and then disrupted using a high-pressure homogenizer (Union Biotech). After centrifugation at 18,000 rpm for 30 min (JA-20 rotor, Beckman Coulter), the supernatant was collected, incubated with Ni^{2+}-Ecel resin (GE Healthcare), and washed with lysis buffer supplemented with 40 mM imidazole. MSP1D1 protein was eluted with elution buffer containing 20 mM Tris-HCl pH 8.0, 150 mM NaCl and 200 mM imidazole, and further purified by SEC (Superdex 200 10/300GL, GE Healthcare) in buffer containing 20 mM Tris-HCl pH 8.0, 150 mM NaCl and 1 mM DTT. The peak fractions were combined and concentrated to 10 mg/mL before storage at −80 °C.

The lipid stock was prepared from a synthetic lipid mixture (POPE:POPS:POPC = 2:1:1, molar ratio; Avanti) together with cholesterol (20% of total mixture, m/m), dissolved in chloroform. The mixture was then dried in a glass test tube under nitrogen flow with gentle rotation for 1 to 2 h. The dried lipid mixture was rehydrated in buffer (20 mM Hepes pH 7.4), and resuspended by cycles of vigorous vertexing and water bath sonication (ultrasonic bath M3800-C, Branson Ultrasonics Corporation). The resulting lipid stock was aliquoted and stored at −80 °C.

GFP-tagged TASK3 was reconstituted into nanodiscs. A thawed aliquot of the lipid stock was clarified by extrusion through a 200 nm polycarbonate filter in a lipid extruder (Avestin LF-1). The reconstitution mixture was assembled by mixing the ingredients in the following order—lipid, DDM (10 mM final concentration), purified TASK3-GFP and MSP1D1, giving a final molar ratio of TASK3-GFP:MSP1D1:lipids = 1:5:450. Incubation at 4 °C for 30 min with gentle rotation was performed each time a new ingredient was added to allow sufficient equilibration. Finally, spontaneous reconstitution of nanodiscs was initiated by the addition of ~500 mg of Bio-Beads SM2 (Bio-Rad; prepared by sequential washing in methanol, water, and buffer containing 20 mM Hepes pH 7.4, 200 mM KCl, 1 mM DTT) and the mixture was incubated overnight at 4 °C with gentle rotation. The next day, Bio-Beads were removed from reconstituted nanodiscs.

To remove empty nanodiscs, reconstituted TASK3 nanodiscs were bound to Streptactin XT resin pre-equilibrated with a detergent-free buffer (20 mM Hepes pH 7.4, 200 mM KCl, and 1 mM DTT) and washed with the same buffer. Nanodiscs on the column were subjected to 3C protease digestion for 5 to 6 h, before the flowthrough was collected and further purified by SEC (Superdex 200 increase GE Healthcare) with desired detergent-free running buffers (neutral and high K^+: 20 mM Hepes pH 7.4 and 200 mM KCl; acidic and high K^+: 30 mM Bis-tris pH 6.0 and 200 mM KCl; acidic and low K^+: 30 mM Bis-tris pH 6.0, 5 mM KCl and 135 mM NaCl; neutral and low K^+: 20 mM Hepes pH 7.4, 5 mM KCl and 135 mM NaCl). The peak fractions were collected and concentrated to 1.0 to 2.0 mg/mL for cryo-EM sample preparation.

Cryo-EM Sample Preparation. Right before grids preparation for cryo-EM studies, TASK3 in nanodiscs was centrifuged at 14,000 rpm for 10 min at 4 °C (Centrifuge 5418R, EPPENDORF). Grids (200 mesh, R1.2/1.3; Quantifoil, Germany) were glow-discharged at 15 mA for 30 s using PELCO easiGlow system. Protein sample (3.5 μL) was applied to grids and incubated for 10 s at 8 °C, 100% humidity, before blotted with filter paper for 3 s and plunge-frozen in liquid ethane cooled by liquid nitrogen using a vitrobot (Vitrobot Mark IV, Thermo Fisher Scientific). Grids were stored under liquid nitrogen until Cryo-EM data acquisition.

Cryo-EM Data Acquisition. Grids were screened in a 200 kV electron microscope (Talos Arctica, Thermo Fisher Scientific) equipped with a direct electron detector (Falcon IV, Thermo Fisher Scientific). Grids giving good image contrast and particle distribution were selected for subsequent data collection using a 300 kV electron microscope (Thermo Fisher Scientific) equipped with a direct electron detector (K3 Summit, Gatan) set to superresolution counting mode. Data collection was performed at ~81,000× magnification, resulting in a magnified physical pixel size of 1.1 Å. Movies were recorded with defocus ranged from 1.5 to 2.5 μm and a total exposure of 50 electrons/$Å^2$ fractionated into 32 frames. The statistics of data collection were summarized in *SI Appendix*, Table S2.

Cryo-EM Data Processing. Cryo-EM datasets collected from samples prepared in different buffer conditions were processed and analyzed using similar procedures. Movies acquired with K3 and Falcon IV detectors were subjected to motion correction for beam-induced drift and binning from superresolution to physical pixel size using MotionCor2 (52) and RELION's own implementation (version: 4.0 beta2), respectively. The contrast transfer function (CTF) parameters for each micrograph were estimated using Gctf (53). Particles were picked by Gautomatch and extracted in RELION (54). Extracted particles were then imported into cryoSPARC (v3.3.2) (55). After rounds of 2D classification, the remaining particles yielded 2D class averages with clear secondary structure features, and were used for ab initio 3D model generation with C2 symmetry in cryoSPARC. The 10 resulting models were used as references in a subsequent cryoSPARC heterogeneous refinement. Particles belonging to classes with canonical K2P features were subjected to cryoSPARC nonuniform refinement. To further improve the resolution, the particles after refinement were exported for Bayesian particle polishing in RELION. Final rounds of nonuniform refinement and local refinement were performed in cryoSPARC to achieve the highest resolutions. Local resolution of the final reconstruction and particle angular distribution were calculated in cryoSPARC. C2 symmetry was imposed throughout all single-particle analyses in 3D. A summary of movie and particle counts for each dataset is included in *SI Appendix*, Table S2.

Modeling and Refinement. All cryo-EM maps were subjected to B-factor sharpening in cryoSPARC prior to structural modeling. An initial TASK3 model was generated by homologous modeling using the TASK1 structure (PDB code: 6RV2) as a template in SWISS-MODEL. Manual adjustments were performed in COOT (56) where map density can reliably correct the initial model, before the structural models were subjected to real-space refinement against the corresponding cryo-EM map in Phenix (57). The refined structures were validated in Molprobity (58), where the stereochemistry and geometry were evaluated. All structural figures in this paper were prepared using PyMOL (59), UCSF ChimeraX (60), and GraphPad Prism 8 and Adobe Illustrator 2023.

Molecular Dynamics Simulation. The TASK3 structures at pH 6.0 and pH 7.4 reported in the paper were used to calculate the residue pKa values and to predict the protonation states of histidine by using the H++ web-server (61). To investigate the effect of histidine protonation, two simulation systems were constructed for TASK3 to individually access protonated and deprotonated states of His98. Disordered loops were modeled using MODELLER (62). These structures were then embedded in a lipid bilayer of POPC (1-palmitoyl-2-oleoyl-sn-glycero-3-phosphocholine) using CHARMM-GUI web-server. In order to create suitable simulation environments, the systems were solvated in water boxes of 100 × 100 × 130 Å, and neutralized with KCl at desired concentrations (5 mM or 200 mM for low or high potassium, respectively). All MD simulations were performed with GROMACS 5.1.4 (63) using the CHARMM36 force field (64). The steepest descent method was applied to minimize

the entire system until energy convergence reached 200.0 kJ/mol/nm. After 50 ns of equilibration, three independent 300-ns production runs were performed for each simulation system with different initial velocities. Throughout the simulations, the NPT ensemble was maintained at a constant temperature of 300 K and a pressure of 1 atm. Temperature control was maintained using the velocity-rescale thermostat. The Parrinello–Rahman barostat with isotropic coupling was used for pressure control. Bond lengths were constrained using the LINCS algorithm with a 2-fs time step. Long-range electrostatic interactions were computed using the Particle Mesh Ewald algorithm with a real-space cutoff of 1.2 nm. Analyses of MD simulations were performed using the GROMACS package version 5.1.4, and plots were generated using the R statistical program version 4.2.2.

Data, Materials, and Software Availability. Cryo-EM density maps (3D reconstructions) and associated structural models data have been deposited in the Electron Microscopy Data Bank (http://www.ebi.ac.uk/pdbe/emdb/) and Protein Data Bank (http://www.rcsb.org) with the accession codes EMD-36793 (65) and PDB-8K1J (66); EMD-36806 (67) and PDB-8K1Z (68); EMD-36805 (69) and PDB-8K1V (70); EMD-36799 (71) and PDB-8K1Q (72). All other data are included in the manuscript and/or *SI Appendix*.

ACKNOWLEDGMENTS. We thank Yafeng Shen, Mi Cao, and staff at the cryo-EM center of Shanghai Institute of Precision Medicine for their assistance with microscope calibration and data collection; Shaobai Li for his advice with cryo-EM data processing. This work was supported by STI2030-Major Project (2022ZD0207000), the National Natural Science Foundation of China (32301002 to H.L., 82273857 to Q.Z., 82373792 to H.Y., and 82101213 to S.C.), Shanghai Rising-Star Program (20QA1405500), the Fundamental Research Funds for the Central Universities (2022JKXYD07001), the Innovative research team of high-level local universities in Shanghai (SHSMU-ZDCX20211201), Shanghai Key Laboratory of Translational Medicine on Ear and Nose Diseases (14DZ2260300), the China National Postdoctoral Program for Innovative Talents (BX2021193) and the startup funding provided by Shanghai Institute of Precision Medicine, Ninth People's Hospital, Shanghai Jiao Tong University School of Medicine (XK2019006). We thank the support of the ECNU Multifunctional Platform for Innovation (001).

Author affiliations: [a]Shanghai Institute of Precision Medicine, Ninth People's Hospital, Shanghai Jiao Tong University School of Medicine, Shanghai 200125, China; [b]Shanghai Key Laboratory of Translational Medicine on Ear and Nose Diseases, Shanghai 200125, China; [c]Shanghai Key Laboratory of Regulatory Biology, Institute of Biomedical Sciences, School of Life Sciences, East China Normal University, Shanghai 200241, China; [d]Department of Otolaryngology-Head and Neck Surgery, Ninth People's Hospital, Shanghai 200011, China; and [e]Ear Institute, Shanghai Jiao Tong University School of Medicine, Shanghai 200125, China

1. Y. Kim, H. Bang, D. Kim, TASK-3, a new member of the tandem pore K^+ channel family. *J. Biol. Chem.* **275**, 9340–9347 (2000), 10.1074/jbc.275.13.9340.
2. C. Karschin *et al.*, Expression pattern in brain of TASK-1, TASK-3, and a tandem pore domain K^+ channel subunit, TASK-5, associated with the central auditory nervous system. *Mol. Cell Neurosci.* **18**, 632–648 (2001), 10.1006/mcne.2001.1045.
3. W. C. Chen, R. L. Davis, Voltage-gated and two-pore-domain potassium channels in murine spiral ganglion neurons. *Hearing Res.* **222**, 89–99 (2006), 10.1016/j.heares.2006.09.002.
4. K. Ryoo, J.-Y. Park, Two-pore domain potassium channels in astrocytes. *Exp. Neurobiol.* **25**, 222–232 (2016), 10.5607/en.2016.25.5.222.
5. X. Wang *et al.*, TASK1 and TASK3 in orexin neuron of lateral hypothalamus contribute to respiratory chemoreflex by projecting to nucleus tractus solitarius. *FASEB J. Off. Publ. Federat. Am. Soc. Exp. Biol.* **35**, e21532 (2021), 10.1096/fj.202002189R.
6. J. H. Choi *et al.*, TWIK-1/TASK-3 heterodimeric channels contribute to the neurotensin-mediated excitation of hippocampal dentate gyrus granule cells. *Exp. Mol. Med.* **50**, 1–13 (2018), 10.1038/s12276-018-0172-4.
7. R. Callahan *et al.*, Immunolocalization of TASK-3 (KCNK9) to a subset of cortical neurons in the rat CNS. *Biochem. Biophys. Res. Commun.* **319**, 525–530 (2004), 10.1016/j.bbrc.2004.05.023.
8. X. Wen *et al.*, Tandem pore domain acid-sensitive K channel 3 (TASK-3) regulates visual sensitivity in healthy and aging retina. *Sci. Adv.* **8**, eabn8785 (2022), 10.1126/sciadv.abn8785.
9. T. K. Baumann, P. Chaudhary, M. E. Martenson, Background potassium channel block and TRPV1 activation contribute to proton depolarization of sensory neurons from humans with neuropathic pain. *Eur. J. Neurosci.* **19**, 1343–1351 (2004), 10.1111/j.1460-9568.2004.03097.x.
10. P. Liao *et al.*, Selective activation of TWIK-related acid-sensitive K^+ 3 subunit-containing channels is analgesic in rodent models. *Sci. Transl. Med.* **11**, eaaw8434 (2019), 10.1126/scitranslmed.aaw8434.
11. C. Morenilla-Palao *et al.*, Ion channel profile of TRPM8 cold receptors reveals a role of TASK-3 potassium channels in thermosensation. *Cell Rep.* **8**, 1571–1582 (2014), 10.1016/j.celrep.2014.08.003.
12. D. J. Langford *et al.*, Variations in potassium channel genes are associated with breast pain in women prior to breast cancer surgery. *J. Neurogenet.* **28**, 122–135 (2014), 10.3109/01677063.2013.856430.
13. M. N. Fullana *et al.*, Selective knockdown of TASK3 potassium channel in monoamine neurons: A new therapeutic approach for depression. *Mol. Neurobiol.* **56**, 3038–3052 (2019), 10.1007/s12035-018-1288-1.
14. M. Borsotto *et al.*, Targeting two-pore domain K^+ channels TREK-1 and TASK-3 for the treatment of depression: A new therapeutic concept. *Br J. Pharmacol.* **172**, 771–784 (2015), 10.1111/bph.12953.
15. L. L. Han *et al.*, Sevoflurane increases hippocampal theta oscillations and impairs memory via TASK-3 channels. *Front Pharmacol.* **12**, 728300 (2021), 10.3389/fphar.2021.728300.
16. O. Barel *et al.*, Maternally inherited Birk Barel mental retardation dysmorphism syndrome caused by a mutation in the genomically imprinted potassium channel KCNK9. *Am. J. Hum. Genet.* **83**, 193–199 (2008), 10.1016/j.ajhg.2008.07.010.
17. M. A. Cousin *et al.*, Gain and loss of TASK3 channel function and its regulation by novel variation cause KCNK9 imprinting syndrome. *Genome Med.* **14**, 62 (2022), 10.1186/s13073-022-01064-4.
18. M. Bedoya *et al.*, TASK channels pharmacology: New challenges in drug design. *J. Med. Chem.* **62**, 10044–10058 (2019), 10.1021/acs.jmedchem.9b00248.
19. W. Gonzalez *et al.*, An extracellular ion pathway plays a central role in the cooperative gating of a K-2P K^+ channel by extracellular pH. *J. Biol. Chem.* **288**, 5984–5991 (2013), 10.1074/jbc.M112.445528.
20. L. Ma, X. Zhang, M. Zhou, H. Chen, Acid-sensitive TWIK and TASK two-pore domain potassium channels change ion selectivity and become permeable to sodium in extracellular acidification. *J. Biol. Chem.* **287**, 37145–37153 (2012), 10.1074/jbc.M112.398164.
21. F. Lesage, J. Barhanin, Molecular physiology of pH-sensitive background K2P channels. *Physiol. (Bethesda)* **26**, 424–437 (2011), 10.1152/physiol.00029.2011.
22. K. E. J. Rodstrom *et al.*, A lower X-gate in TASK channels traps inhibitors within the vestibule. *Nature* **582**, 443–447 (2020), 10.1038/s41586-020-2250-8.
23. L. G. Cuello, V. Jogini, D. M. Cortes, E. Perozo, Structural mechanism of C-type inactivation in K^+ channels. *Nature* **466**, 203–208 (2010), 10.1038/nature09153.
24. T. Hoshi, W. N. Zagotta, R. W. Aldrich, Two types of inactivation in Shaker K^+ channels: Effects of alterations in the carboxy-terminal region. *Neuron* **7**, 547–556 (1991), 10.1016/0896-6273(91)90367-9.
25. Y. M. Leung, Involvement of C-type inactivation gating in the actions of voltage-gated K^+ channel inhibitors. *Pharmacol. Therapeutics* **133**, 151–158 (2012), 10.1016/j.pharmthera.2011.10.005.
26. R. Reddi, K. Matulef, E. A. Riederer, M. R. Whorton, F. I. Valiyaveetil, Structural basis for C-type inactivation in a Shaker family voltage-gated K^+ channel *Sci. Adv.* **8**, eabm8804 (2022), 10.1126/sciadv.abm8804.
27. J. F. Cordero-Morales *et al.*, Molecular determinants of gating at the potassium-channel selectivity filter. *Nat. Struct. Mol. Biol.* **13**, 311–318 (2006), 10.1038/nsmb1069.
28. Y. Zhou, J. H. Morais-Cabral, A. Kaufman, R. MacKinnon, Chemistry of ion coordination and hydration revealed by a K^+ channel-Fab complex at 2.0 A resolution. *Nature* **414**, 43–48 (2001), 10.1038/35102009.
29. T. Hoshi, C. M. Armstrong, C-type inactivation of voltage-gated K^+ channels: Pore constriction or dilation? *J. General Physiol.* **141**, 151–160 (2013), 10.1085/jgp.201210888.
30. M. Lolicato *et al.*, K2P channel C-type gating involves asymmetric selectivity filter order-disorder transitions. *Sci. Adv.* **6**, eabc9174 (2020), 10.1126/sciadv.abc9174.
31. V. Pau, Y. Zhou, Y. Ramu, Y. Xu, Z. Lu, Crystal structure of an inactivated mutant mammalian voltage-gated K^+ channel. *Nat. Struct. Mol. Biol.* **24**, 857–865 (2017), 10.1038/nsmb.3457.
32. J. López-Barneo, T. Hoshi, S. H. Heinemann, R. W. Aldrich, Effects of external cations and mutations in the pore region on C-type inactivation of Shaker potassium channels. *Receptors & Channels* **1**, 61–71 (1993).
33. T. Baukrowitz, G. Yellen, Modulation of K^+ current by frequency and external [K^+]: A tale of two inactivation mechanisms. *Neuron* **15**, 951–960 (1995), 10.1016/0896-6273(95)90185-x.
34. L. G. Cuello *et al.*, Structural basis for the coupling between activation and inactivation gates in K^+ channels. *Nature* **466**, 272–275 (2010), 10.1038/nature09136.
35. W. Kopec, B. S. Rothberg, B. L. de Groot, Molecular mechanism of a potassium channel gating through activation gate-selectivity filter coupling. *Nat. Commun.* **10**, 5366 (2019), 10.1038/s41467-019-13227-w.
36. J. Yan, Q. Li, R. W. Aldrich, Closed state-coupled C-type inactivation in BK channels. *Proc. Natl. Acad. Sci. U.S.A.* **113**, 6991–6996 (2016), 10.1073/pnas.1607584113.
37. B. Li, R. A. Rietmeijer, S. G. Brohawn, Structural basis for pH gating of the two-pore domain K^+ channel TASK2. *Nature* **586**, 457–462 (2020), 10.1038/s41586-020-2770-2.
38. T. S. Turney, V. Li, S. G. Brohawn, Structural Basis for pH-gating of the K^+ channel TWIK1 at the selectivity filter. *Nat. Commun.* **13**, 3232 (2022), 10.1038/s41467-022-30853-z.
39. M. Lolicato *et al.*, K2P2.1 (TREK-1)-activator complexes reveal a cryptic selectivity filter binding site. *Nature* **547**, 364–368 (2017), 10.1038/nature22988.
40. S. G. Brohawn, J. del Marmol, R. MacKinnon, Crystal structure of the human K2P TRAAK, a lipid- and mechano-sensitive K^+ ion channel. *Science* **335**, 436–441 (2012), 10.1126/science.1213808.
41. A. N. Miller, S. B. Long, Crystal structure of the human two-pore domain potassium channel K2P1. *Science* **335**, 432–436 (2012), 10.1126/science.1213274.
42. Y. Y. Dong *et al.*, K2P channel gating mechanisms revealed by structures of TREK-2 and a complex with Prozac. *Science* **347**, 1256–1259 (2015), 10.1126/science.1261512.
43. Q. Kuang, P. Purhonen, H. Hebert, Structure of potassium channels. *Cell Mol. Life Sci.* **72**, 3677–3693 (2015), 10.1007/s00018-015-1948-5.
44. Q. Zhang *et al.*, "C-type" closed state and gating mechanisms of K2P channels revealed by conformational changes of the TREK-1 channel. *J. Mol. Cell Biol.* **14**, mjac002 (2022), 10.1093/jmcb/mjac002.
45. S. Rajan *et al.*, TASK-3, a novel tandem pore domain acid-sensitive K^+ channel. An extracellular histiding as pH sensor. *J. Biol. Chem.* **275**, 16650–16657 (2000), 10.1074/jbc.M000030200.
46. G. Czirjak, P. Enyedi, TASK-3 dominates the background potassium conductance in rat adrenal glomerulosa cells. *Mol. Endocrinol.* **16**, 621–629 (2002), 10.1210/mend.16.3.0788.
47. P. A. M. Schmidpeter *et al.*, Membrane phospholipids control gating of the mechanosensitive potassium leak channel TREK1. *Nat. Commun.* **14**, 1077 (2023), 10.1038/s41467-023-36765-w.

48. S. G. Brohawn, E. B. Campbell, R. MacKinnon, Physical mechanism for gating and mechanosensitivity of the human TRAAK K^+ channel. *Nature* **516**, 126–130 (2014), 10.1038/nature14013.
49. R. A. Rietmeijer, B. Sorum, B. Li, S. G. Brohawn, Physical basis for distinct basal and mechanically gated activity of the human K^+ channel TRAAK. *Neuron* **109**, 2902–2913.e2904 (2021), 10.1016/j.neuron.2021.07.009.
50. A. M. Natale, P. E. Deal, D. L. Minor Jr., Structural insights into the mechanisms and pharmacology of K2P potassium channels. *J. Mol. Biol.* **433**, 166995 (2021), 10.1016/j.jmb.2021.166995.
51. A. Goehring *et al.*, Screening and large-scale expression of membrane proteins in mammalian cells for structural studies. *Nat. Protoc.* **9**, 2574–2585 (2014), 10.1038/nprot.2014.173.
52. S. Q. Zheng *et al.*, MotionCor2: Anisotropic correction of beam-induced motion for improved cryo-electron microscopy. *Nat. Methods* **14**, 331–332 (2017), 10.1038/nmeth.4193.
53. K. Zhang, Gctf: Real-time CTF determination and correction. *J. Struct. Biol.* **193**, 1–12 (2016), 10.1016/j.jsb.2015.11.003.
54. J. Zivanov *et al.*, New tools for automated high-resolution cryo-EM structure determination in RELION-3. *eLife* **7**, e42166 (2018), 10.7554/eLife.42166.
55. A. Punjani, J. L. Rubinstein, D. J. Fleet, M. A. Brubaker, cryoSPARC: Algorithms for rapid unsupervised cryo-EM structure determination. *Nat. Methods* **14**, 290–296 (2017), 10.1038/nmeth.4169.
56. P. Emsley, B. Lohkamp, W. G. Scott, K. Cowtan, Features and development of Coot. *Acta Crystallogr. D Biol. Crystallogr.* **66**, 486–501 (2010), 10.1107/s0907444910007493.
57. P. D. Adams *et al.*, PHENIX: A comprehensive Python-based system for macromolecular structure solution. *Acta Crystallogr. D Structural Biol.* **66**, 213–221 (2010), 10.1107/S0907444909052925.
58. C. J. Williams *et al.*, MolProbity: More and better reference data for improved all-atom structure validation. *Protein Sci. Publ. Protein Soc.* **27**, 293–315 (2018), 10.1002/pro.3330.
59. B. H. M. Mooers, M. E. Brown, Templates for writing PyMOL scripts. *Protein Sci. Publ. Protein Soc.* **30**, 262–269 (2021), 10.1002/pro.3997.
60. E. F. Pettersen *et al.*, UCSF ChimeraX: Structure visualization for researchers, educators, and developers. *Protein Sci.* **30**, 70–82 (2020), 10.1002/pro.3943.
61. J. C. Gordon *et al.*, H++: A server for estimating pKas and adding missing hydrogens to macromolecules. *Nucleic Acids Res.* **33**, W368–W371 (2005), 10.1093/nar/gki464.
62. N. Eswar *et al.*, Comparative protein structure modeling using MODELLER. *Curr. Protoc. Protein Sci.* **50**, 2.9.1–2.9.31 (2007), 10.1002/0471140864.ps0209s50.
63. M. J. Abraham *et al.*, GROMACS: High performance molecular simulations through multi-level parallelism from laptops to supercomputers. *SoftwareX* **1**, 19–25 (2015), 10.1016/j.softx.2015.06.001.
64. J. Huang, A. D. MacKerell, CHARMM36 all-atom additive protein force field: Validation based on comparison to NMR data. *J. Comput. Chem.* **34**, 2135–2145 (2013), 10.1002/jcc.23354.
65. H. Lin *et al.*, the cryo-EM map of TASK3 at pH 7.4 and 200 mM KCl. EMDB. https://www.ebi.ac.uk/emdb/EMD-36793. Deposited 11 July 2023.
66. H. Lin *et al.*, the atomic coordinates of TASK3 at pH 7.4 and 200 mM KCl. PDB. https://www.rcsb.org./structure/8K1J. Deposited 11 July 2023.
67. H. Lin *et al.*, the cryo-EM map of TASK3 at pH 6.0 and 200 mM KCl. EMDB. https://www.ebi.ac.uk/emdb/EMD-36806. Deposited 11 July 2023.
68. H. Lin *et al.*, the atomic coordinates of TASK3 at pH 6.0 and 200 mM KCl. PDB. https://www.rcsb.org./structure/8K1Z. Deposited 11 July 2023.
69. H. Lin *et al.*, the cryo-EM map of TASK3 at pH 7.4, 5 mM KCl and 135 mM NaCl. EMDB. https://www.ebi.ac.uk/emdb/EMD-36805. Deposited 11 July 2023.
70. H. Lin *et al.*, the atomic coordinates of TASK3 at pH 7.4, 5 mM KCl and 135 mM NaCl. PDB. https://www.rcsb.org./structure/8K1V. Deposited 11 July 2023.
71. H. Lin *et al.*, the cryo-EM map of TASK3 at pH 6.0, 5 mM KCl and 135 mM NaCl. EMDB. https://www.ebi.ac.uk/emdb/EMD-36799. Deposited 11 July 2023.
72. H. Lin *et al.*, the atomic coordinates of TASK3 at pH 6.0, 5 mM KCl and 135 mM NaCl. PDB. https://www.rcsb.org./structure/8K1Q. Deposited 11 July 2023.